The Role of Electrochemical Phenomena in Scanning Probe Microscopy of Ferroelectric Thin Films

Sergei V. Kalinin,* Stephen Jesse, Alexander Tselev, Arthur P. Baddorf, and Nina Balke

Oak Ridge National Laboratory, Oak Ridge, Tennessee 37831, United States

ABSTRACT Applications of piezoresponse force microscopy and conductive atomic force microscopy to ferroelectric thin films necessitate understanding of the possible bias-induced electrochemical reactivity of oxide surfaces. These range from reversible ionic surface charging (possibly coupled to polarization) and vacancy and proton injection to partially reversible vacancy ordering, to irreversible electrochemical degradation of the film and bottom electrode. Here, the electrochemical phenomena induced by a biased tip are analyzed and both theoretical and experimental criteria for their identification are summarized.

KEYWORDS: scanning probe microscopy · ferroelectric thin films · electrochemical phenomena · oxides

In recent years, much attention has been attracted to nanoscale phenomena in ferroelectric films as explored by pezoresponse frce mcroscopy (PFM) and conductive AFM (cAFM). The notable examples include ferroelectric domain patterning,[1−3] dynamic studies,[4−7] and polarization-mediated electronic transport.[8−11] With few exceptions,[10,12−15] these studies are performed in ambient environment and include applications of high voltage stresses to the films. Under these conditions, a broad spectrum of electrochemical phenomena is possible, ranging from trivial charging of surface water layers (note that ionic charges such as H^+ and OH^- cannot relax though bulk electronic conduction and relaxation necessitates surface or bulk ionic flows), ionic exchange between material and liquid (*e.g.*, for $LiNbO_3$),[16] to solid state electrochemical reactions affecting the bulk of material. The latter can range from reversible injection of oxygen vacancies, to vacancy ordering, to formation of new oxygen-deficient phases and cation demixing.[17] While not explored in the context of PFM, the recent work on memristive and electroresistive phenomena in titanates,[18−21] as well as similarity between ferroelectric oxides and materials used in solid oxide fuel cells,[22−24] points to the potential importance of ionic and electrochemical phenomena in these materials.

Recently, a number of groups have reported the role of surface charges in voltage-modulated SPM[25] and PFM[26,27] and their effect on observed domain wall evolution. However, much less attention was paid to the role of bulk electrochemical phenomena in PFM and cAFM of ferroelectric and other perovskite films (in comparison with, *e.g.*, scanning tunneling microscopy[28,29]). Last year, it was shown that dislocation injections in materials such as $SrTiO_3$ (STO) from aqueous interfaces is possible at voltages as low as 3−4 V.[30] Combined with the near-universal presence of a water droplet at the tip−surface junction,[31,32] this necessitates the search for (a) experimental signatures of the tip-induced electrochemical processes and (b) materials-based criteria to estimate the probability of electrochemical (*vs* intrinsic physical) mechanisms.

Phenomenological Observations of Electrochemical Phenomena in PFM. To illustrate the preponderance of electrochemical phenomena in PFM measurements, several representative examples are shown in Figure 1. In Figure 1a, the surface topography of ∼30 nm thick lead zirconate titanate (PZT) film after application of ∼5 V bias in the high-humidity (∼80−90%) atmosphere is illustrated. The formation of surface corrugation of 1−2 nm scale (comparable to the step edge height) is clearly visible. As another example, shown in Figure 1b is the PFM phase image (contrast ∼10°) on the nominally 0.4 nm PZT film on STO substrate. At this thickness, the film is expected to be nonferroelectric, but the PFM indicates clear phase variation. The corresponding hysteresis loop (not shown) is reminiscent of minor hysteresis loops for ferroelectric materials. Notably, the extremely small thickness of the film suggests that the presence of ferroelectric polarization is highly unlikely, and observed anomalous PFM contrast is due to ionic responses. Similarly, bias-induced piezoelectric contrast

* Address correspondence to sergei2@ornl.gov.

Received for review April 12, 2011 and accepted June 17, 2011.

Published online June 18, 2011
10.1021/nn2013518

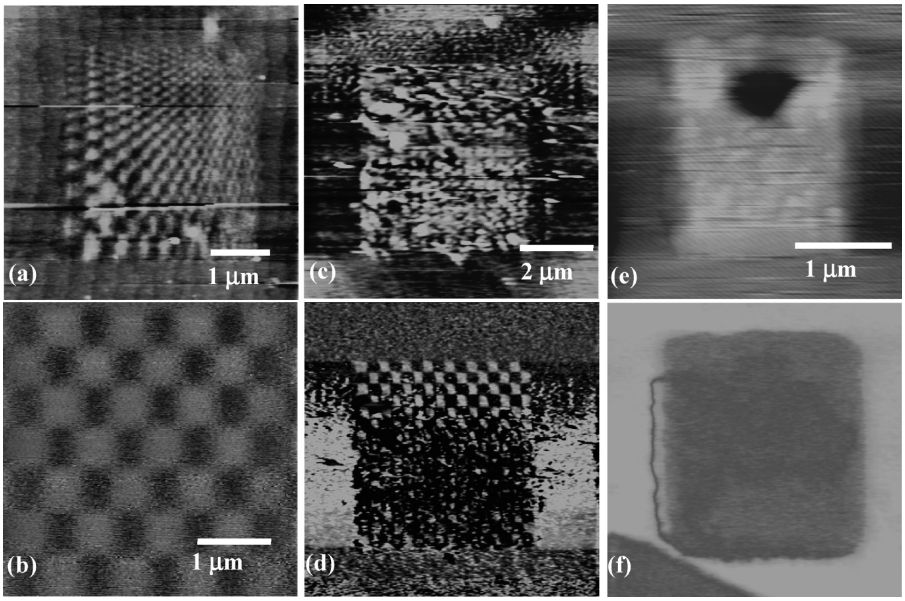

Figure 1. (a) Surface topography of PZT film after PFM-based domain writing. Vertical scale is 5 nm. (b) Phase PFM image of nominally 0.4 nm PZT film. Scale is 10°. (c) Surface topography and (d) PFM amplitude image of the PZT film after domain writing under high-humidity conditions. (e) Surface topography and (f) PFM amplitude image of $BiFeO_3$ ceramic surface after ~20 scan switching by −10 V.

was observed in nonferroelectric oxides including $(La_xSr_{1-x})MnO_3$,[33,34] $SrTiO_3$,[34] and $CaCu_3Ti_4O_{12}$,[35] where electrochemical phenomena could partly contribute to the measured response. Figure 1c,d illustrates a more drastic example of surface damage on the PZT surface induced by application of ±8 V in the checkerboard pattern. Notably, a clear PFM image is visible in the top third of the image despite extreme damage to the material. Finally, Figure 1e,f demonstrates damage induced by repeated scanning with a biased SPM tip on $BiFeO_3$ ceramics, which in this case is associated with suppression of PFM contrast.[36]

To establish a possible mechanism of the surface damage, we illustrate the correlation of surface damage, polarization switching, and electronic current for 30 nm PZT/LSMO/STO heterostructures (LSMO stands for $La_{0.3}Sr_{0.7}MnO_3$). Figure 2a shows the sample topography after poling a 1 × 1 μm^2 area with 6 V bias. The poling induced a height increase (material swelling) in the poled area by 3−4 nm, while maintaining the general characteristics of the as-grown surface morphology. This behavior can be interpreted as either vacancy injection in a purely oxygen reduction/evolution reaction $2O_O^x \leftrightarrow 2V_x^{\bullet\bullet} + O_2 + 4e'$ or proton injection, $H^+ + e^- \leftrightarrow H_i \leftrightarrow H_i' + e'$, where Kröger−Vink notation for defects is used.[17] Alternatively, more extensive damage including nanodischarges or injection of extended defects similar to ref 30, is possible. The link between vacancy density and molar volume is universal for all oxides ranging from ceria[37] to cobaltites,[38−41] nickelates,[42] titanates, and manganites.[43] We note that systematic material transfer from the tip (beyond small tip degradation) can be largely excluded since no continuous degradation of image quality is observed after repetitive scanning, whereas topographical changes indicate significant amounts of deposited material and uniform expansion of material within the scanned region. For the same reasons, the changes in surface topography induced by ferroelastic switching[44,45] of multiaxial ferroelectric can be excluded.

Poling a smaller square with −6 V amplitude on top of the damaged surface and recording PFM signal afterward (Figure 2b,c) demonstrates that the film remains ferroelectric despite the topography change and despite the fact that the PFM amplitude decreased in the damaged region. The second poling did not induce any further surface change. A similar experiment was repeated with single point measurements on a 5 × 5 grid in a 1 × 1 μm^2 area (Figure 2d−f). At each point, the ferroelectric response was measured (1 V_{ac}, 890 kHz) as a function of voltage up to 6 V. Figure 2g−i illustrates measured ferroelectric hysteresis loops (amplitude, phase, and mixed PFM signal). Notably, the PFM images and the ferroelectric hysteresis loop show what might be classified as "normal" ferroelectric switching.

The described behavior was observed on several samples of different thicknesses and compositions. Generally, thinner samples (≤30 nm) always show changes in topography, whereas for thicker samples the probability for surface damage is strongly reduced. Furthermore, similar samples do not show any surface damage if measured in ultrahigh vacuum (UHV)[10,12] even for film thicknesses down to 2 nm, implicating the facilitating role of the water meniscus in

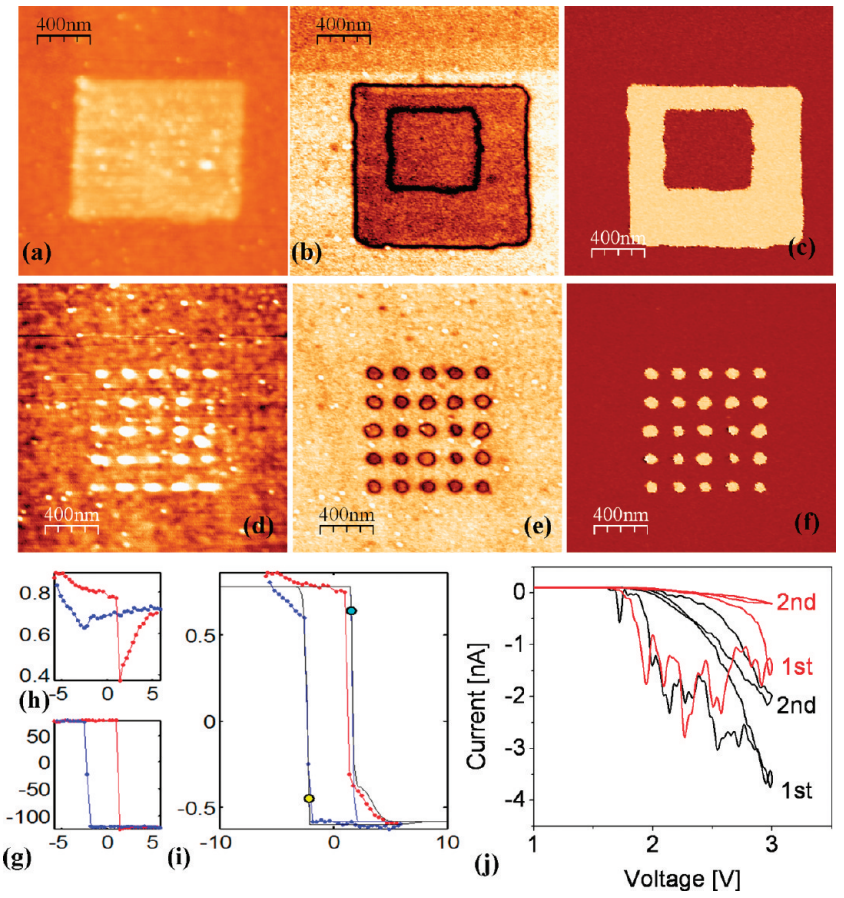

Figure 2. (a) Surface topography of a PZT film after domain poling with 6 V. Vertical scale is 16 nm. (b) Amplitude and (c) phase PFM images after back poling with −6 V (inner square). Scales are 2 and 20 V, respectively. (d) Surface topography of PZT film after a 5 × 5 grid of bipolar voltage pulses to measure ferroelectric switching hysteresis with a maximum voltage of 6 V. Vertical scale is 2 nm. (e) Amplitude and (f) phase PFM images after locally applied voltage pulses. Scales are 3.7 and 20 V, respectively. (g) PFM amplitude, (h) phase, and (i) PFM mixed signal measured for a single point measured during the grid experiment shown in panels d−f. (j) Current measurements on two single points with two voltage sweeps each.

electrochemical reactivity, similar to SPM-based nanooxidation[46−48] and nanostructure formation.[49] Unipolar experiments have shown that the surface damage is only induced under positive voltages applied to the tip, consistent with oxygen vacancy injection. Furthermore, this behavior is strongly correlated with locally measured *I*−*V* curves, which show current only for voltages larger than +1.5 V, as shown in Figure 2j. The surface damage is induced when positive voltages are applied to the tip during the first voltage sweep, which is accompanied by large electrical current spikes. The second voltage sweep shows much smaller currents and smooth *I*−*V* curves without spikes.

Theoretical Analysis of Electrochemical Phenomena at the Tip−Surface Junction. To estimate the propensity of the material for tip-induced electrochemical process, we consider the process driven by the generation/annihilation of electroactive species (oxygen vacancies, protons, hydroxyls) at the tip−surface junction with subsequent diffusion or migration driven transport through the film. The essential part of this model is the presence of a potential drop in the tip−surface junction (previously considered in the context of a dielectric dead layer effect in PFM[50]), which drives the electrochemical process. This voltage divider model is illustrated in Figure 3.

The self-consistent model of tip-induced electrochemical reaction requires the relationships between the potential drop in the tip−surface junction and the reaction rate and between the potential drop in the material and the ionic and electronic fluxes through the material. While development of general model is clearly challenging (and for scenarios involving, *e.g.*, spatial separation of metallic tip and electrochemical reaction zone, the lumped element modeling is inapplicable), we note that (a) ferroelectric materials are typically poor ionic conductors at room temperature but can support electronic leakage currents,[51] and (b) in ambient, a water droplet is present at the tip−surface junction. From (a), the potential drop in the bulk can be ascribed to electronic resistance only, providing a readily measurable parameter in cAFM. From (b), the interfacial reaction kinetics (or rate) can be modeled as a Butler−Volmer (BV) process[52] (while in the water-free environment, the choice of BV *vs* Nernstian kinetics is still actively debated[53]). In this

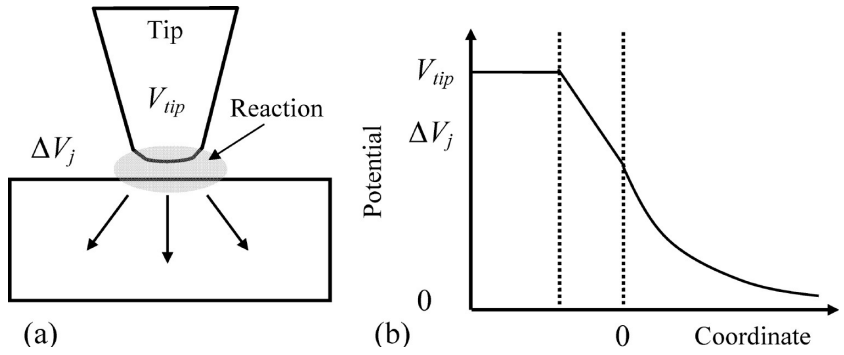

Figure 3. (a) Schematic of the electrochemical processes at the tip−surface junction. Application of the bias, V_{tip}, to the SPM probe leads to potential drops in the tip−surface junction and in the bulk, $V_{tip} = \Delta V_j + \Delta V_b$. The potential drop in the junction can drive electrochemical reactions and generate mobile ionic species that redistribute under the combined effect of electric field and concentration gradients. (b) Potential distribution under the tip *vs* distance coordinate along the tip axis. Note that the potential drop in the bulk will be a nonlinear function of the coordinate even in the absence of ionic and electronic screening as a consequence of the localized nature of the probe. The electric field will be enhanced under the tip.

case, the ionic current generated at the junction is related to the potential drop across the interface as

$$I_{ion} = I_0\left(\exp\left(\frac{\alpha_a F\Delta E}{RT}\right) - \exp\left(-\frac{\alpha_c F\Delta E}{RT}\right)\right) \quad (1)$$

where α_a and α_c are anodic and cathodic charge transfer coefficients, respectively, F is the Faraday constant, R is the gas constant, T is the temperature, ΔE is the overpotential (difference between the potential drop at the junction and the equilibrium redox potential or the reaction), and I_0 is the exchange current density. While the BV parameters (particularly I_0) are generally not available for oxide−gas or oxide−water systems at room temperature, as an estimate, we use typical values for oxide fuel cell materials. Extrapolating the temperature dependence of exchange current for the Pd-yttria-stabilized zirconia system,[54] we obtain $I_0 = 2.5 \times 10^{-10}$ A and $\alpha_a \approx \alpha_c \approx 0.5$. While the authors do not provide the surface area, estimating it as ~1 cm^2 yields exchange current densities of $i_0 = 2.5 \times 10^{-6}$ A/m^2.

The voltage divider model illustrated in Figure 3 allows the relationship between the potential drops at the junction and in the bulk as

$$\pi R_{tip}^2 i_0 \sinh\left(\frac{FV_j}{2RT}\right) + \frac{V_j}{R_e} = I_b \quad (2)$$

where $I_b(V) = I_b(V_{tip} - V_j)$ is the current though the bulk determined by the potential drop in the bulk, and R_{tip} is tip−surface contact radius. R_e is the electronic resistance of the junction assumed to be parallel to ionic resistance. We note that while the exact values of R_e are unknown, since I−V measurements cannot decouple junction and bulk resistance, and impedance-based methods do not provide sufficient sensitivity for decoupling interface and bulk contributions in SPM configuration,[55] estimates can be obtained by measurements using nominally blocking electrodes on conductive materials with similar chemistries (*e.g.*, strongly doped $SrTiO_3$ *vs* thin nonconductive $SrTiO_3$ films on conductive substrates).

While a realistic transport mechanism can be utilized to yield the numerical solution of eq 2, here we consider the simplified cases of (a) known current density and (b) uniform bulk conductance: $I_b = (V_{tip} - V_j)R_{tip}\sigma$, where σ is the specific conductivity of the material.

Shown in Figure 4 are the potential drops in the tip−surface junction, that is, the overpotential driving the electrochemical reaction, for several values of electronic tip−surface resistance, R_e calculated for known current densities (case (a)). For low electronic junction resistances, the potential drop in the junction is essentially zero for moderate currents (below a few microamperes) and electrochemical processes are unlikely. At the same time, the presence of an insulating layer on the surface combined with high bias stresses induces electrochemical reactivity and injection of ionic species in material. The effect of the exchange current is illustrated in Figure 3b for I_0 reduced by the factor of $\beta = 10^{-6}$ and 10^{-3}. Note that the effect on the critical current density is relatively weak (due to the strong exponential dependence in eq 1), and hence uncertainties in electrochemical reactivity will have only a logarithmically small effect on dynamics.

As a second comparison, shown in Figure 4c,d are potential drops in tip−surface junction as a function of bulk specific resistance. Note that for highly conductive materials (*e.g.*, for doped $SrTiO_3$, $\rho = 0.017\ \Omega\cdot$cm[56]) with nonconductive surfaces the potential drops in the junction and hence electrochemical reactivity could be significant, whereas for nonconductive materials, the potential drops predominantly through the bulk. This behavior is further illustrated in Figure 4d, describing the effect of surface electronic resistance.

While our model illustrates that the prerequisites for electrochemistry, namely, water and a potential difference across the tip−surface junction, are readily available under a biased tip in an ambient environment,

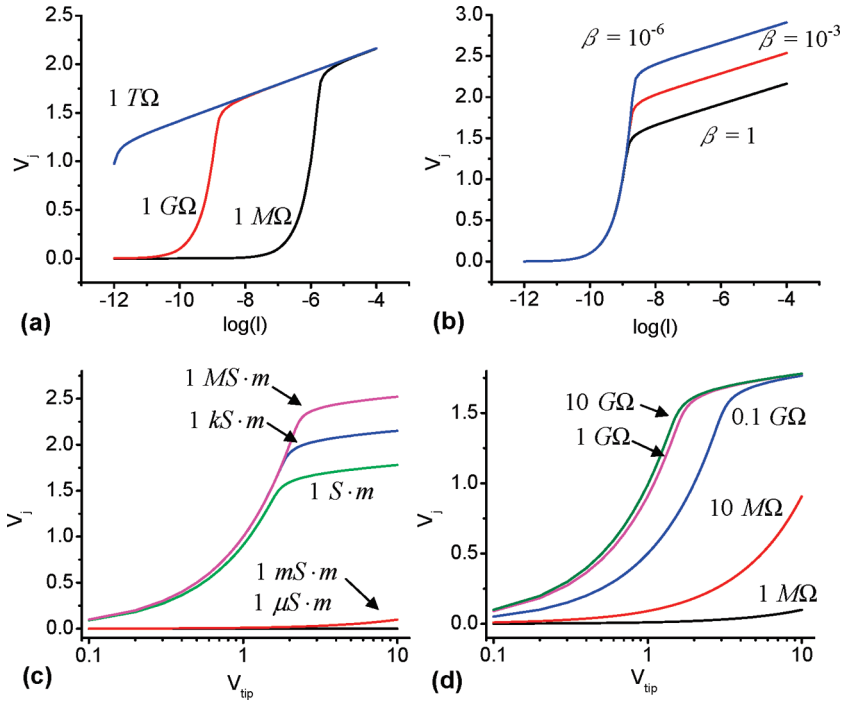

Figure 4. Potential drop in the tip−surface junction as a function of current for (a) $i_0 = 2.5 \times 10^{-6}$ A/m^2 and different R_e and (b) R_e= 1 GΩ and different β. Potential drop in the tip−surface junction for (c) R_e = 1 GΩ and different σ and (d) σ = 1 S/m and different R_e.

several real-world conditions may enhance these effects. First is the presence of contaminants on the surface and in the water droplet, increasing the ionic conductivity of the liquid. Even well-prepared surfaces are susceptible to contaminations by hydrocarbons, sulfides, and chlorides abundantly present in ambient atmosphere. Adsorbed on the surface, their concentration can be significant in the small volume of water under at tip. Second, as in any electrochemistry, the tip material can contribute actively to the process, acting as a catalyst.

Thermal Effects at the Tip−Surface Junction. An additional factor in conductive SPM measurements will be the Joule heating of the material, tip, and water by high current densities at the tip−surface junction. The effects can be manifold and include (a) thermal removal of water and contaminants from the tip−surface junction (thus improving the contact), (b) thermal activation of bias-induced processes including polarization switching and electrochemical reaction, and (c) thermal expansion of the material which will be detected in the SPM signal. To estimate the thermal and thermomechanical effects induced by the current flow, we utilize the direct numerical simulations using COMSOL finite elements analysis package (COMSOL v4.1) with a simplified geometry of a disk electrode on a material with a fixed bulk resistance assuming zero heat transfer on the top surface and electrode. Shown in Figure 5a,b are the relevant stationary temperature and displacement distribution. Note that the temperature distribution extends in the material at a length scale comparable to the tip radius, as can be expected from the diffusive nature of the heat transport. At the same time, the mechanical displacement is strongly localized below the tip due to $1/r$ behavior of the corresponding strain Green's function. The temperature and maximal displacement *versus* current curves are shown in Figure 5c,d. Note that in this case $I \sim V\sigma$, where V is applied bias and σ is conductivity, allowing direct parametrization of the response. From Figure 5c,d, currents below 100 nA are not expected to produce significant thermal or mechanical effects; however, a few microampere currents will lead to significant temperatures (ΔT > 100 K) at the tip−surface junction. We further note that given that temperature and thermomechanical displacement are quadratic in voltage, $\Delta T \sim V^2$, these effects will not contribute to the first harmonic of the signal measured in PFM at zero dc tip bias (only second harmonic of the signal affected (unpublished)) but will contribute to the measurements in the dc field (*e.g.*, PFM spectroscopy) similar to electrostriction effects.

General Factors Affecting Electrochemical Phenomena in PFM. The universal feature of the experimentally observed behaviors in Figures 1 and 2 and analyses in Figure 4 is that a combination of high leakage current, low bulk conductivity, and the presence of low electronic conductivity at tip−surface junction results in the significant surface potential drops and overpotentials necessary to drive electrochemical processes, giving rise to a broad range of physical and electrochemical

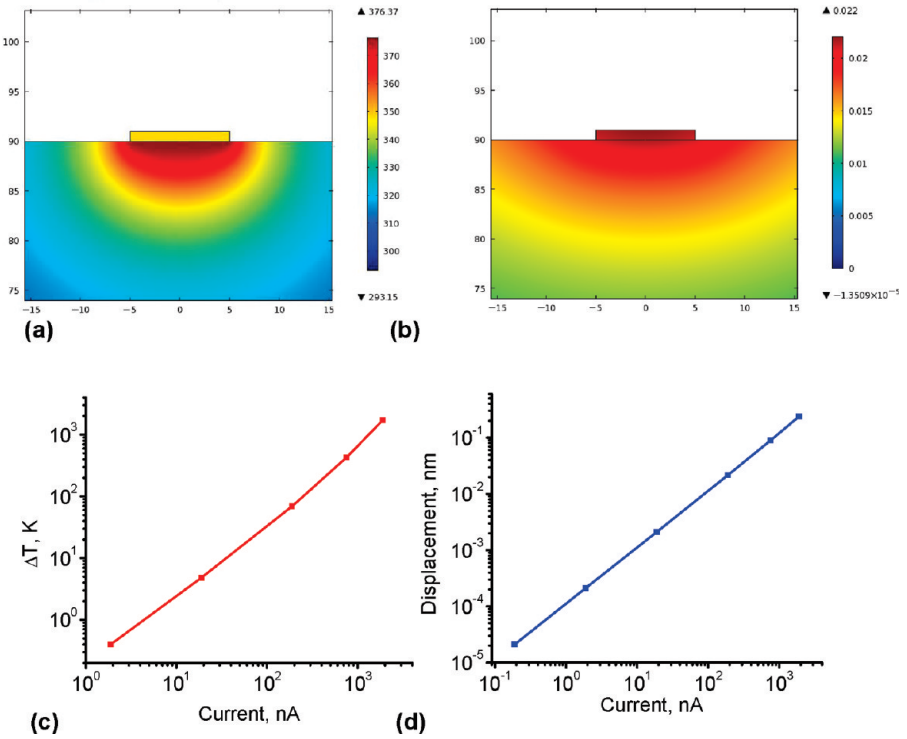

Figure 5. Thermal effects induced by current flow. (a) Temperature and (b) mechanical displacement below a circular electrode with 10 nm radius and with bulk conductivity of 0.45 S/m. Current dependence of the (c) maximal temperature under the electrode and (d) maximal surface displacement.

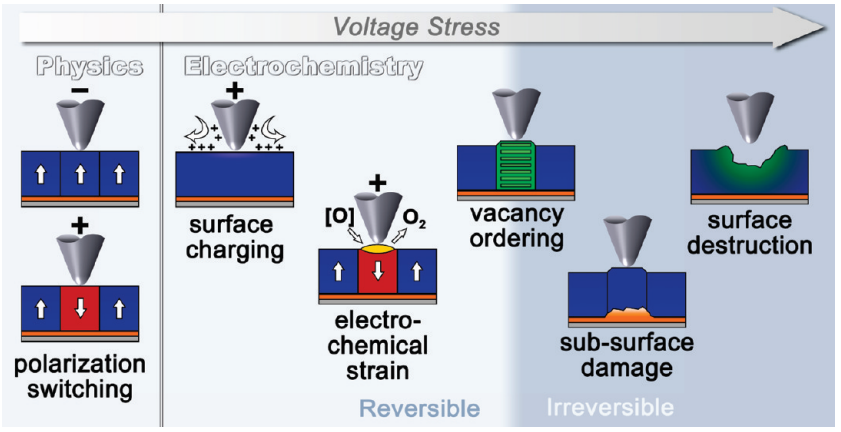

Figure 6. Bias-induced reversible and irreversible phenomena under the SPM tip. For illustration, the phenomena are divided in physical (not involving ionic motion) and electrochemical (involving ionic motion).

phenomena, as depicted in Figure 6. The purely physical phenomena include polarization switching, which may be associated with a charge-specific adsorption[57] that stabilizes the ferroelectric state[58–60] or surface charging by mobile ions[25,61] that contribute to the depolarization field. Note that spreading of screening surface charges is now argued to be the factor controlling domain switching and back-switching kinetics in PFM.[26,27] Interestingly, similar phenomena are now argued to underpin the metal insulator transitions in oxide heterostructures,[62,63] pointing to universality of these mechanisms.

Activation of surface electrochemical reactions can lead to oxygen vacancies, proton and hydroxyl injection, and annihilation, each associated with changes of molar volume of host material (and hence mechanical effects). These processes do not affect the continuity of oxygen and cation sublattices and hence can be reversible. Further effects include oxygen vacancy ordering (that can be both reversible and irreversible), as well as irreversible processes that destroy the crystalline lattice, including surface damage, cation demixing, degradation at the bottom electrode, or dielectric breakdown. While many of these phenomena have not

yet been explored for perovskites, recent studies of Li-ion conduction materials,[64,65] oxygen ion conductors,[66] and a large body of available data on ferroelectrics allow the following characteristic signatures of these processes to be formulated.

The reversible injection of oxygen vacancies (or protons) associated with changes of the molar volume of material cannot be differentiated from the piezoelectric effect based on PFM data alone. The difficulty in distinction is somewhat similar to that between electrets and ferroelectrics based on P-E loop measurements. Reversible ionic motion can give rise to a time relaxation of the signal (on the scale of the corresponding diffusion times) and (kinetically induced) hysteresis loops. Absence of relaxation phenomena over a broad time range (10^{-4} to 10^{2} s) is strong evidence against ionic dynamics; in contrast, the presence of relaxation can be a consequence of ionic motion, relaxor-type polarization dynamics,[67−69] or domain wall motion below the tip.

In comparison, irreversible motion of oxygen vacancies (*e.g.*, associated with ordering) in the film or bottom electrode, injection of large-scale defects, and phase transformations can be identified through the (a) anomalous bias-dependent PFM contrast, (b) broad domain walls, and (c) topographic changes on the film surfaces. For example, in classical ferroelectrics, the PFM signal will adopt a +PR value in positive domains and −PR value in the negative domains. In the ionic process, the contrast will be a continuous function of writing voltage (similar to domain writing in ferroelectric relaxors). Furthermore, transients in the hysteresis loops (where first loop and subsequent loops are different, or loops are not closed) are a strong indicator of electrochemical response. Finally, even minute topographic changes (sometimes below the unit cell level) are a strong indicator of the onset of an irreversible electrochemical process. Given the typical chemical expansion coefficients of transition metal oxides, a ∼10% vacancy accumulation will lead to a ∼1% change in molar volume,[38,41] providing a relationship between surface expansion and penetration depth of electrochemically transformed region. For example, for a 10 nm film surface, deformations on the order of ∼0.1−0.3 nm will be consistent with irreversible vacancy accumulation, whereas stronger changes will be indicative of amorphization or injection of extended defects. We further note that for ultrathin films the damage can also accumulate in the bottom electrode, especially for materials such as $(La_xSr_{1-x})CoO_3$ with good ionic conductivity and tendency for amorphization.[70]

Electrochemical phenomena are less of a concern for bulk ferroelectric materials and single crystals, where the potential drop occurs primarily through the bulk. High-quality contamination-free surfaces and good tip−surface contacts also reduce these effects. Imaging in vacuum and dry atmosphere will suppress electrochemical reactivity since electrochemical splitting of water molecules is kinetically much more favorable then the four-electron oxygen reduction/evolution reaction of the type $2O_O^x \leftrightarrow 2V_x^{\bullet\bullet} + O_2 + 4e'$ and equivalent redox potentials are lower. Similarly, the use of large current-limiting resistors can significantly reduce electrochemical surface damage. However, combined transport PFM experiments on even moderately conductive films will be highly susceptible to electrochemical reactions, as can be expected given the similarity between these materials and electroresistive systems. Interestingly, similar issues arise in the context of molecular electronic systems, where ionic phenomena can also contribute to observed transport behaviors.[71] Finally, electrochemical effects can also be expected in nonferroelectric materials (*e.g.*, systems such as manganites, cobaltites, *etc.*) and for thick ferroelectrics under high-field conditions, such as capacitors and tunneling junctions, where the ionic motion could be a major contributor to electric field-induced strain. The latter, in turn, can affect effective barrier width in tunneling experiments, result in memristive ionic switching, *etc.*, necessitating these phenomena to be differentiated from intrinsic polarization switching effects.

METHODS

Piezoresponse force microscopy (PFM) imaging, domain switching, and current measurements were performed on a commercial SPM system (Veeco Dimension and Veeco Multimode). For imaging, a typical ac voltage of 1−2 V_{pp} at 30−100 kHz and a maximum switching voltage of ±9 V was applied to the SPM tip during the measurement. Metal-coated tips (Au and Pt) from a number of manufacturers (MicroMash, Veeco) were used.

Acknowledgment. This research was conducted at the Center for Nanophase Materials Sciences, which is sponsored at Oak Ridge National Laboratory by the Office of Basic Energy Sciences, U.S. Department of Energy. The authors gratefully acknowledge H.N. Lee (ORNL), P. Yu (UC Berkeley), and P.K. Davies (UPenn) for samples used in these studies over past decade, and P. Maksymovych (ORNL), F. Ciucci (Heidelberg), A. Kholkin (U. Aveiro), A. Morozovska (UAS), and A. Gruverman (UNL) for invaluable discussions.

REFERENCES AND NOTES

1. Tybell, T.; Ahn, C. H.; Triscone, J. M. Ferroelectricity in Thin Perovskite Films. *Appl. Phys. Lett.* **1999**, *75*, 856–858.
2. Liu, X.; Terabe, K.; Nakamura, M.; Takekawa, S.; Kitamura, K. Nanoscale Chemical Etching of Near-Stoichiometric Lithium Tantalate. *J. Appl. Phys.* **2005**, *97*, 064308-4.
3. Gruverman, A.; Kholkin, A. Nanoscale Ferroelectrics: Processing, Characterization and Future Trends. *Rep. Prog. Phys.* **2006**, *69*, 2443–2474.

4. Tybell, T.; Paruch, P.; Giamarchi, T.; Triscone, J. M. Domain Wall Creep in Epitaxial Ferroelectric $Pb(Zr_{0.2}Ti_{0.8})O_3$ Thin Films. *Phys. Rev. Lett.* **2002**, *89*, 097601.
5. Rodriguez, B. J.; Nemanich, R. J.; Kingon, A.; Gruverman, A.; Kalinin, S. V.; Terabe, K.; Liu, X. Y.; Kitamura, K. Domain Growth Kinetics in Lithium Niobate Single Crystals Studied by Piezoresponse Force Microscopy. *Appl. Phys. Lett.* **2005**, *86*, 012906-3.
6. Pertsev, N. A.; Petraru, A.; Kohlstedt, H.; Waser, R.; Bdikin, I. K.; Kiselev, D.; Kholkin, A. L. Dynamics of Ferroelectric Nanodomains in $BaTiO_3$ Epitaxial Thin Films *via* Piezoresponse Force Microscopy. *Nanotechnology* **2008**, *19*, 375703.
7. Kalinin, S. V.; Morozovska, A. N.; Chen, L. Q.; Rodriguez, B. J. Local Polarization Dynamics in Ferroelectric Materials. *Rep. Prog. Phys.* **2010**, *73*, 056502.
8. Garcia, V.; Fusil, S.; Bouzehouane, K.; Enouz-Vedrenne, S.; Mathur, N. D.; Barthélémy, A.; Bibes, M. Giant Tunnel Electroresistance for Non-destructive Readout of Ferroelectric States. *Nature* **2009**, *460*, 81–84.
9. Gruverman, A.; Wu, D.; Lu, H.; Wang, Y.; Jang, H. W.; Folkman, C. M.; Zhuravlev, M. Y.; Felker, D.; Rzchowski, M.; Eom, C. B.; *et al.* Tunneling Electroresistance Effect in Ferroelectric Tunnel Junctions at the Nanoscale. *Nano Lett.* **2009**, *9*, 3539–3543.
10. Maksymovych, P.; Jesse, S.; Yu, P.; Ramesh, R.; Baddorf, A. P.; Kalinin, S. V. Polarization Control of Electron Tunneling into Ferroelectric Surfaces. *Science* **2009**, *324*, 1421–1425.
11. Seidel, J.; Martin, L. W.; He, Q.; Zhan, Q.; Chu, Y. H.; Rother, A.; Hawkridge, M. E.; Maksymovych, P.; Yu, P.; Gajek, M.; *et al.* Conduction at Domain Walls in Oxide Multiferroics. *Nat. Mater.* **2009**, *8*, 229–234.
12. Maksymovych, P.; Balke, N.; Jesse, S.; Huijben, M.; Ramesh, R.; Baddorf, A.; Kalinin, S. Defect-Induced Asymmetry of Local Hysteresis Loops on $BiFeO_3$ Surfaces. *J. Mater. Sci.* **2009**, *44*, 5095–5101.
13. Liu, X.; Kitamura, K.; Terabe, K. Surface Potential Imaging of Nanoscale $LiNbO_3$ Domains Investigated by Electrostatic Force Microscopy. *Appl. Phys. Lett.* **2006**, *89*, 132905-3.
14. Peter, F.; Szot, K.; Waser, R.; Reichenberg, B.; Tiedke, S.; Szade, J. Piezoresponse in the Light of Surface Adsorbates: Relevance of Defined Surface Conditions for Perovskite Materials. *Appl. Phys. Lett.* **2004**, *85*, 2896–2898.
15. Zeng, H. R.; Yin, Q. R.; Li, G. R.; Luo, H. S.; Xu, Z. K. Abnormal Piezoresponse Behavior of $Pb(Mg_{1/3}Nb_{2/3})O_3$-30%$PbTiO_3$ Single Crystal Studied by High-Vacuum Scanning Force Microscope. *J. Cryst. Growth* **2003**, *254*, 432–436.
16. Laurell, F.; Roelofs, M. G.; Hsiung, H. Loss of Optical Nonlinearity in Proton-Exchanged $LiNbO_3$ Waveguides. *Appl. Phys. Lett.* **1992**, *60*, 301–303.
17. Maier, J. *Physical Chemistry of Ionic Materials: Ions and Electrons in Solids*; Wiley: New York, 2004.
18. Tsuruoka, T.; Terabe, K.; Hasegawa, T.; Aono, M. Forming and Switching Mechanisms of a Cation-Migration-Based Oxide Resistive Memory. *Nanotechnology* **2010**, *21*, 425205.
19. Waser, R.; Aono, M. Nanoionics-Based Resistive Switching Memories. *Nat. Mater.* **2007**, *6*, 833–840.
20. Sawa, A. Resistive Switching in Transition Metal Oxides. *Mater. Today* **2008**, *11*, 28–36.
21. Strukov, D. B.; Snider, G. S.; Stewart, D. R.; Williams, R. S. The Missing Memristor Found. *Nature* **2008**, *453*, 80–83.
22. Bagotsky, V. S. *Fuel Cells: Problems and Solutions*; Wiley: New York, 2009.
23. O'Hayre, R.; Cha, S. W.; Colella, W.; Prinz, F. B. *Fuel Cell Fundamentals*; Wiley: New York, 2009.
24. Kharton, V. V., Ed. *Solid State Electrochemistry I: Fundamentals, Materials and Their Applications*; Wiley-VCH: New York, 2009.
25. Kalinin, S. V.; Bonnell, D. A. Screening Phenomena on Oxide Surfaces and Its Implications for Local Electrostatic and Transport Measurements. *Nano Lett.* **2004**, *4*, 555–560.
26. Dahan, D.; Molotskii, M.; Rosenman, G.; Rosenwaks, Y. Ferroelectric Domain Inversion: The Role of Humidity. *Appl. Phys. Lett.* **2006**, *89*, 152902-3.
27. Kholkin, A.; Bdikin, I. K.; Shvartsman, V. V.; Pertsev, N. A. Anomalous Polarization Inversion in Ferroelectrics *via* Scanning Force Microscopy. *Nanotechnology* **2007**, *18*, 095502.
28. Fan, F.-R. F.; Bard, A. J.; Guckenberger, R.; Heim, M. STM on Wet Insulators: Electrochemistry or Tunneling?. *Science* **1995**, *270*, 1849–1852.
29. Freund, J.; Halbritter, J.; Hörber, J. K. H. How Dry Are Dried Samples? Water Adsorption Measured by STM. *Microsc. Res. Tech.* **1999**, *44*, 327–338.
30. Ueno, K.; Shimotani, H.; Iwasa, Y.; Kawasaki, M. Electrostatic Charge Accumulation *versus* Electrochemical Doping in $SrTiO_3$ Electric Double Layer Transistors. *Appl. Phys. Lett.* **2010**, *96*, 252107-3.
31. Weeks, B. L.; Vaughn, M. W.; DeYoreo, J. J. Direct Imaging of Meniscus Formation in Atomic Force Microscopy Using Environmental Scanning Electron Microscopy. *Langmuir* **2005**, *21*, 8096–8098.
32. Scovell, D. L.; Pinkerton, T. D.; Finlayson, B. A.; Stuve, E. M. The Dielectric Response of Water in High Electric Fields: Equilibrium Water Thickness and the Field Distribution. *Chem. Phys. Lett.* **1998**, *294*, 255–261.
33. Mamin, R. F.; Bdikin, I. K.; Kholkin, A. L. Locally Induced Charged States in $La_{0.89}Sr_{0.11}MnO_3$ Single Crystals. *Appl. Phys. Lett.* **2009**, *94*, 222901-3.
34. Kholkin, A.; Bdikin, I.; Ostapchuk, T.; Petzelt, J. Room Temperature Surface Piezoelectricity in $SrTiO_3$ Ceramics *via* Piezoresponse Force Microscopy. *Appl. Phys. Lett.* **2008**, *93*, 222905-3.
35. Tararam, R.; Bdikin, I.; Varela, J. A.; Bueno, P. R.; Gracio, J.; Kholkin, A. Local Electromechanical Properties of the $CaCu_3Ti_4O_{12}$ Ceramics. *Mater. Res. Soc. Symp. Proc.* **2010**, *1255*, M03-19.
36. Kalinin, S. V. Nanoscale Electric Phenomena at Oxide Surfaces and Interfaces by Scanning Probe Microscopy. Ph.D. Thesis, University of Pennsylvania, 2002.
37. Bishop, S. R.; Duncan, K. L.; Wachsman, E. D. Defect Equilibria and Chemical Expansion in Non-stoichiometric Undoped and Gadolinium-Doped Cerium Oxide. *Electrochim. Acta* **2009**, *54*, 1436–1443.
38. Adler, S. B. Chemical Expansivity of Electrochemical Ceramics. *J. Am. Ceram. Soc.* **2001**, *84*, 2117–2119.
39. Zuev, A. Y.; Vylkov, A. I.; Petrov, A. N.; Tsvetkov, D. S. Defect Structure and Defect-Induced Expansion of Undoped Oxygen Deficient Perovskite $LaCoO_{3-\delta}$. *Solid State Ionics* **2008**, *179*, 1876–1879.
40. Lein, H. L.; Wiik, K.; Grande, T. Thermal and Chemical Expansion of Mixed Conducting $La_{0.5}Sr_{0.5}Fe_{1-x}Co_xO_{3-\delta}$ Materials. *Solid State Ionics* **2006**, *177*, 1795–1798.
41. Chen, X.; Yu, J.; Adler, S. B. Thermal and Chemical Expansion of Sr-Doped Lanthanum Cobalt Oxide ($La_{1-x}Sr_xCoO_{3-\delta}$). *Chem. Mater.* **2005**, *17*, 4537–4546.
42. Kharton, V. V.; Kovalevsky, A. V.; Avdeev, M.; Tsipis, E. V.; Patrakeev, M. V.; Yaremchenko, A. A.; Naumovich, E. N.; Frade, J. R. Chemically Induced Expansion of $La_2NiO_{4+\delta}$-Based Materials. *Chem. Mater.* **2007**, *19*, 2027–2033.
43. Zuev, A. Y.; Tsvetkov, D. S. Oxygen Nonstoichiometry, Defect Structure and Defect-Induced Expansion of Undoped Perovskite $LaMnO_{3\pm\delta}$. *Solid State Ionics* **2010**, *181*, 557–563.
44. Chen, L.; Ouyang, J.; Ganpule, C. S.; Nagarajan, V.; Ramesh, R.; Roytburd, A. L. Formation of 90° Elastic Domains During Local 180° Switching in Epitaxial Ferroelectric Thin Films. *Appl. Phys. Lett.* **2004**, *84*, 254–256.
45. Vasudevan, R. K.; Chen, Y.-C.; Tai, H.-H.; Balke, N.; Wu, P.; Bhattacharya, S.; Chen, L. Q.; Chu, Y.-H.; Lin, I. N.; Kalinin, S. V.; *et al.* Exploring Topological Defects in Epitaxial $BiFeO_3$ Thin Films. *ACS Nano* **2011**, *5*, 879–887.
46. Cambel, V.; Soltys, J. The Influence of Sample Conductivity on Local Anodic Oxidation by the Tip of Atomic Force Microscope. *J. Appl. Phys.* **2007**, *102*, 074315-7.
47. Dagata, J. A.; Inoue, T.; Itoh, J.; Matsumoto, K.; Yokoyama, H. Role of Space Charge in Scanned Probe Oxidation. *J. Appl. Phys.* **1998**, *84*, 6891–6900.
48. Bartošík, M.; Škoda, D.; Tomanec, O.; Kalousek, R.; Jánský, P.; Zlámal, J.; Spousta, J.; Dub, P.; Šikola, T. Role of Humidity in Local Anodic Oxidation: A Study of Water Condensation

and Electric Field Distribution. *Phys. Rev. B* **2009**, *79*, 195406.
49. Qiu, H.; Lu, Y.-F.; Mai, Z.-H. Nanostructure Formation on Amorphous WO_3 Thin Films in Air by Scanning Tunneling Microscopy. *Jpn. J. Appl. Phys., Part 1* **2001**, *40*, 290–294.
50. Kalinin, S. V.; Bonnell, D. A. Temperature Dependence of Polarization and Charge Dynamics on the $BaTiO_3$(100) Surface by Scanning Probe Microscopy. *Appl. Phys. Lett.* **2001**, *78*, 1116–1118.
51. Scott, J. F. *Ferroelectric Memories*; Springer: Heidelberg, Germany, 2000.
52. Bard, A. J.; Faulkner, L. R. *Electrochemical Methods: Fundamentals and Applications*; John Wiley & Sons: New York, 2001.
53. Adler, S. B. Factors Governing Oxygen Reduction in Solid Oxide Fuel Cell Cathodes. *Chem. Rev.* **2004**, *104*, 4791–4844.
54. Athanasiou, C.; Karagiannakis, G.; Zisekas, S.; Stoukides, M. Electrode Polarization at the O_2(G), Pd/YSZ Interface. *Solid State Ionics* **2000**, *136*−*137*, 873–877.
55. Shao, R.; Kalinin, S. V.; Bonnell, D. A. Local Impedance Imaging and Spectroscopy of Polycrystalline ZnO Using Contact Atomic Force Microscopy. *Appl. Phys. Lett.* **2003**, *82*, 1869–1871.
56. Johnson, K. D.; Dravid, V. P. Static and Dynamic Electron Holography of Electrically Active Grain Boundaries in $SrTiO_3$. *Interface Sci.* **2000**, *8*, 189–198.
57. Kalinin, S. V.; Bonnell, D. A. Effect of Phase Transition on the Surface Potential of the $BaTiO_3$ (100) Surface by Variable Temperature Scanning Surface Potential Microscopy. *J. Appl. Phys.* **2000**, *87*, 3950–3957.
58. Fong, D. D.; Kolpak, A. M.; Eastman, J. A.; Streiffer, S. K.; Fuoss, P. H.; Stephenson, G. B.; Thompson, C.; Kim, D. M.; Choi, K. J.; Eom, C. B.; *et al.* Stabilization of Monodomain Polarization in Ultrathin $PbTiO_3$ Films. *Phys. Rev. Lett.* **2006**, *96*, 127601.
59. Wang, R. V.; Fong, D. D.; Jiang, F.; Highland, M. J.; Fuoss, P. H.; Thompson, C.; Kolpak, A. M.; Eastman, J. A.; Streiffer, S. K.; Rappe, A. M.; *et al.* Reversible Chemical Switching of a Ferroelectric Film. *Phys. Rev. Lett.* **2009**, *102*, 047601.
60. Shin, J.; Nascimento, V. B.; Geneste, G.; Rundgren, J.; Plummer, E. W.; Dkhil, B.; Kalinin, S. V.; Baddorf, A. P. Atomistic Screening Mechanism of Ferroelectric Surfaces: An *In Situ* Study of the Polar Phase in Ultrathin $BaTiO_3$ Films Exposed to H_2O. *Nano Lett.* **2009**, *9*, 3720–3725.
61. Cunningham, S.; Larkin, I. A.; Davis, J. H. Noncontact Scanning Probe Microscope Potentiometry of Surface Charge Patches: Origin and Interpretation of Time-Dependent Signals. *Appl. Phys. Lett.* **1998**, *73*, 123–125.
62. Bi, F.; Bogorin, D. F.; Cen, C.; Bark, C. W.; Park, J.-W.; Eom, C.-B.; Levy, J. "Water-Cycle" Mechanism for Writing and Erasing Nanostructures at the $LaAlO_3/SrTiO_3$ Interface. *Appl. Phys. Lett.* **2010**, *97*, 173110-3.
63. Xie, Y.; Bell, C.; Hikita, Y.; Hwang, H. Y. Tuning the Electron Gas at an Oxide Heterointerface *via* Free Surface Charges. *Adv. Mater.* **2011**, *23*, 1744–1747.
64. Balke, N.; Jesse, S.; Morozovska, A. N.; Eliseev, E.; Chung, D. W.; Kim, Y.; Adamczyk, L.; Garcia, R. E.; Dudney, N.; Kalinin, S. V. Nanoscale Mapping of Ion Diffusion in a Lithium-Ion Battery Cathode. *Nat. Nanotechnol.* **2010**, *5*, 749–754.
65. Balke, N.; Jesse, S.; Kim, Y.; Adamczyk, L.; Tselev, A.; Ivanov, I. N.; Dudney, N. J.; Kalinin, S. V. Real Space Mapping of Li-Ion Transport in Amorphous Si Anodes with Nanometer Resolution. *Nano Lett.* **2010**, *10*, 3420–3425.
66. Kumar, A.; Ciucci, F.; Morozovska, A. N.; Kalinin, S. V.; Jesse, S. Measuring Oxygen Reduction/Evolution Reactions on the Nanoscale. *Nat. Chem.* **2011**, submitted.
67. Kalinin, S. V.; Rodriguez, B. J.; Jesse, S.; Morozovska, A. N.; Bokov, A. A.; Ye, Z. G. Spatial Distribution of Relaxation Behavior on the Surface of a Ferroelectric Relaxor in the Ergodic Phase. *Appl. Phys. Lett.* **2009**, *95*, 142902-3.
68. Shvartsman, V. V.; Kholkin, A. L.; Tyunina, M.; Levoska, J. Relaxation of Induced Polar State in Relaxor $PbMg_{1/3}Nb_{2/3}O_3$ Thin Films Studied by Piezoresponse Force Microscopy. *Appl. Phys. Lett.* **2005**, *86*, 222907-3.
69. Kholkin, A.; Bdikin, I.; Kiselev, D.; Shvartsman, V.; Kim, S. H. Nanoscale Characterization of Polycrystalline Ferroelectric Materials for Piezoelectric Applications. *J. Electroceram.* **2007**, *19*, 83–96.
70. Kubicek, M.; Limbeck, A.; Fromling, T.; Hutter, H.; Fleig, J. Relationship between Cation Segregation and the Electrochemical Oxygen Reduction Kinetics of $La_{0.6}Sr_{0.4}CoO_{3-\delta}$ Thin Film Electrodes. *J. Electrochem. Soc.* **2011**, *133*, 941–948.
71. Yao, J.; Zhong, L.; Natelson, D.; Tour, J. M. Silicon Oxide: A Non-innocent Surface for Molecular Electronics and Nanoelectronics Studies. *J. Am. Chem. Soc.* **2011**, *133*, 941–948.